

Fast multipole accelerated boundary element methods for room acoustics

Nail A. Gumerov* and Ramani Duraiswami†
 Perceptual Interfaces and Reality Lab, UMIACS,
 University of Maryland, College Park, MD
 Also at VisiSonics Corporation, College Park, MD

March 31, 2021

Abstract

The direct and indirect boundary element methods, accelerated via the fast multipole method, are applied to numerical simulation of room acoustics for large rooms of volume $\sim 150 m^3$ and frequencies up to 5 kHz on a workstation. As the parameter kD (wavenumber times room diameter) is large, stabilization of the previously developed FMM algorithms is required for accuracy. A stabilization scheme is one of the key contribution of this paper. The computations are validated using well-known image source solutions for shoebox shaped rooms. Computations for L-shaped rooms are performed to illustrate the ability to capture diffractions. The ability to model in-room baffles, and boundary openings (doors/windows) is also demonstrated. The largest case has $kD > 1100$ with a discretization of size 6 million elements. The performance of different boundary integral formulations was compared, and their rates of convergence using a preconditioned flexible GMRES were found to be substantially different. These promising results suggest a path to efficient simulations of room acoustics via high performance boundary element methods.

1 Introduction

The perception of sound by humans, and the computational simulation of acoustic propagation leading to such perception, have been the subject of many studies. The simulation models the propagation of sound from the source location to the receiver – a microphone or the ears of a listener. The setting may be a real source in a real environment – indoors or outdoors, or a virtual environment – in a game or extended reality simulation. The simulation is often performed in two independent pieces – first the multipath propagation of the sound from the source to the location of the receiver, and second the scattering of the incoming sound off the anatomy en route to the ear canal of the listener.

The equations governing acoustic propagation is the linear wave equation neglecting dispersion. Time invariant (or slowly varying) systems can be usefully characterized by an impulse response, which can then be used with convolution to compute the sound field for arbitrary sources. The scattering off the anatomy can be characterized by the head related impulse response (HRIR), and the scattering off the room walls and other obstacles by the point-to-point room impulse response (RIR). The overall binaural room impulse response (BRIR) can be obtained via a compositional model from these [ZDD04].

This work is concerned with the computation of the room impulse response using fast multipole accelerated boundary element (FMMBEM) methods. A previous paper used FMMBEM to compute the HRIR [GODZ10]. Once the response is computed it can be put to various uses – e.g., used in an *audio*

*ngumerov@umd.edu, <https://www.umiacs.umd.edu/users/gumerov>

†ramanid@umd.edu, <https://www.umiacs.umd.edu/users/ramani>

engine for rendering 3D audio, e.g., in a game or virtual reality application [RS18]; or used to assess the listening properties of a space such as a concert hall or a meeting room; or assess, via simulation, architectural choices of room shapes and materials [Kut16].

Among methods for the solution of the wave equation are approximate geometric methods that rely on tracing of rays, or groups of rays. Such approaches are more popular (and more accurate for) light propagation but can be adapted to acoustics [FTC⁺04, SS15]. These methods can be augmented with approaches that approximately account for wave effects such as diffraction and diffuse reflections [SMM14, PCD20]. The methods can quickly get leading order effects in an explainable fashion. However, when used to obtain the whole impulse response, they suffer from combinatorial explosion when the propagation process has many interactions of waves with surfaces, and with each other (caustics). Moreover, it is not possible to provide an accuracy bound or a computational cost bound for achieving a given numerical accuracy. Further, it may not be possible to enforce realistic boundary conditions. On the other hand, these methods allow for simple geometries to be computed efficiently (e.g., via images [AB79, Bor84]). Moreover, the methods allow taking large time steps as the wavefront is propagated. Finally, because of the development of GPU based raytracing approaches, there is promise for fast execution on modern computers.

In contrast the methods that solve the wave equation can usually provide an error and computational cost bounds, as well as the ability to enforce correct boundary conditions. The wave equation can be solved in time and space variables over the entire domain. This is done in discretization of its original form via finite differences [HB17], finite-volume [BHBS16] or spectral-element methods [RNL09], or finite element methods [OYSO16]. A key parameter that enters into the accuracy of the simulation is the smallest wavelength that must be resolved (or equivalently the highest frequency). The Nyquist criterion requires at least two discretization points (or elements or degrees of freedom) per wavelength (λ), while in practice this number is six to ten for accuracy. In three dimensions, this means that if the average linear dimension is D , and the wavenumber $k (= 2\pi/\lambda)$, the number of variables in the discretization is $N \simeq O(kD)^3$.

The goal of these simulations is to obtain the response due to an impulsive source at a particular location. The duration of the simulation Y is the length of the impulse response – the time taken for a unit impulse to die down to negligible levels. When the equation is solved via a time marching method, with an average time step size h , the number of steps is T/h . When a linear system is solved at each step, the cost of the solution will be proportional to $O(N)^\alpha$. For a direct solve via LU decomposition the value of α is 3. If sparsity or other properties can be used to control the cost of the solution, either via an iterative Krylov method or a fast direct method, the value of α can be reduced to 2, or even lower to 1 using specialized direct methods, which are an item of research. So, the overall cost of computation can be reduced to $O(T/h)(kD)^{3\alpha}$.

These global methods have several other pros and cons. They can solve more generalized versions of the wave equation (e.g., with dispersion, and variable sound speeds). Moreover, once the solution is completed, the pressure and velocity are known throughout the field. On the other hand, the methods cannot handle infinite domains (with radiation conditions) easily; though this is not necessary for internal acoustics problems. The treatment of curved boundaries, or those with corners can lead to errors. Finally, it is not straightforward to incorporate frequency dependent parameters in boundary conditions.

The wave equation is often solved in the Fourier domain, which leads to the Helmholtz equation for each frequency component, and the frequency response is obtained instead of the impulse response. While, in principle, we need to solve this equation over an infinite band of frequencies, we only need to obtain the complex response at $T/2h$ frequencies to compute the impulse response. While the Helmholtz equation can also be solved via domain discretization using the finite difference or finite element methods, in this paper we seek to solve it via the boundary element method. For the BEM we only need to discretize the boundary of the domain leading to $N \simeq O(kD)^2$ sized discretization, with dense matrices.

Note that for room acoustics the value of kD can be relatively large – from a few hundreds to tens of thousands, depending on the dimensions of the room and the maximum frequency considered. Because the discretization size varies as a power of this parameter (as the cube for domain methods, or as the square for boundary methods), the resulting linear systems are very large, and the time taken for setting up the linear system, as well as for their solution is significant, unless fast algorithms are used. We explore two variants of the boundary-element method, the direct [GD09] and the indirect boundary

element method [GAD13], in Sections 3.1 and 3.2.

Using the fast-multipole method for accelerating matrix-vector products that occur in Krylov iterative methods for solving the linear systems can significantly reduce the time and memory needed for solution. For the high values of kD that are encountered in room acoustics, the translation and rotation operators in the FMM [GD09, GODZ10] were found to be inaccurate due to instabilities in the recursion procedures that are used. We propose in Section 3.3 new stable translation and rotation procedures that are stable at higher kD . Also, we compare the integral equation formulations for their convergence rates, and find that some formulations are more optimal. We achieve solutions with $O(kD)^2$ memory and $O(kD)^{2\alpha}$ time, with $1 \leq \alpha < 2$. Results on sample problems are shown, and possible directions for future work indicated. Based on these results we believe FMM accelerated BEM is a promising approach for accurate and fast room acoustics simulations for practical room sizes and frequency ranges.

2 Statement of the problem

We consider a room bound by closed or open surface S (the walls, ceiling, and floor, possibly with some openings and some internal baffled surfaces). Assume that the inhomogeneity of the air due to the temperature gradient is negligible and the propagation of sound can be described by the wave equation with a constant speed of sound, c ,

$$\frac{\partial^2 p(\mathbf{r}, t)}{\partial t^2} = c^2 \nabla^2 p(\mathbf{r}, t), \quad (1)$$

where p is the acoustic pressure depending on time t and the radius-vector \mathbf{r} or a point in the room. Furthermore, we consider time-periodic signals with period T . The Fourier transform in time domain results in the Helmholtz equation for each harmonic component,

$$\nabla^2 \psi(\mathbf{r}; k) + k^2 \psi(\mathbf{r}; k) = 0, \quad k = \omega/c, \quad (2)$$

where ψ is the complex amplitude of the sound pressure, ω is the circular frequency. Assume further that the room boundaries are locally reacting surface, whose properties do not depend on the angle of sound incidence, so the following boundary conditions can be imposed [Kut16]

$$-\zeta(\mathbf{r}; k) \frac{\partial \psi}{\partial n} + ik\psi \Big|_S = 0. \quad (3)$$

The normal to S is assumed directed outside the room, ζ is the specific impedance, which is complex, and related to the wall reflection (R) and absorption (α) coefficients as

$$\zeta(\mathbf{r}; k) = \frac{1 + R(\mathbf{r}; k)}{1 - R(\mathbf{r}; k)}, \quad \alpha(\mathbf{r}; k) = 1 - |R(\mathbf{r}; k)|^2. \quad (4)$$

For fully absorbing surfaces ($R = 0$, $\alpha = 1$), $\zeta = 1$. For sound hard surfaces ($R = 1$, $\alpha = 0$), $\zeta = \infty$, boundary condition (3) is replaced by the Neumann condition

$$\frac{\partial \psi}{\partial n} \Big|_S = 0. \quad (5)$$

Due to linearity of the problem it is sufficient to obtain a solution for a single monopole source of unit intensity located at some point \mathbf{r}_s as more complex incident fields can be simulated by integration over prescribed source distributions. Thus, we consider

$$\psi(\mathbf{r}; k) = \psi^{in}(\mathbf{r}; k) + \psi^{sc}(\mathbf{r}; k), \quad \psi^{in} = G_k(\mathbf{r}, \mathbf{r}_s) = \frac{e^{ik|\mathbf{r}-\mathbf{r}_s|}}{4\pi|\mathbf{r}-\mathbf{r}_s|}, \quad (6)$$

where ψ^{in} and ψ^{sc} are the incident and the scattered fields, and $G_k(\mathbf{r}, \mathbf{r}_s)$ is the Green's function for the Helmholtz equation with wavenumber k . The field ψ^{sc} has no singularity inside the room and can be computed using boundary conditions

$$\frac{\partial \psi^{sc}}{\partial n} + \frac{k}{i\zeta(\mathbf{r}; k)} \psi^{sc} \Big|_S = \gamma(\mathbf{r}; k) = - \left(\frac{\partial \psi^{in}}{\partial n} + \frac{k}{i\zeta(\mathbf{r}; k)} \psi^{in} \right) \Big|_S, \quad (7)$$

Note that a solution ψ obtained for such a formulation satisfies in the domain

$$\nabla^2 \psi(\mathbf{r}; k) + k^2 \psi(\mathbf{r}; k) = -\delta(\mathbf{r}, \mathbf{r}_s). \quad (8)$$

3 Method of solution

3.1 Direct BEM

When the room surface S is closed, the direct boundary element method based on the use of Green's identity for internal points can be used,

$$\psi^{sc}(\mathbf{r}, k) = L_k \left[\frac{\partial \psi^{sc}}{\partial n} \right] (\mathbf{r}) - M_k [\psi^{sc}] (\mathbf{r}), \quad \mathbf{r} \notin S, \quad (9)$$

where L_k and M_k are the single and double layer potentials,

$$\begin{aligned} L_k [\sigma] (\mathbf{r}) &= \int_S \sigma(\mathbf{r}') G_k(\mathbf{r}, \mathbf{r}') dS(\mathbf{r}'), \\ M_k [\mu] (\mathbf{r}) &= \int_S \mu(\mathbf{r}') \frac{\partial}{\partial n(\mathbf{r}')} G_k(\mathbf{r}, \mathbf{r}') dS(\mathbf{r}'). \end{aligned} \quad (10)$$

The surface values of the scattered field can be found by applying the limiting form of Green's identity (9), which for smooth surfaces yields

$$\frac{1}{2} \psi^{sc}(\mathbf{r}, k) = L_k \left[\frac{\partial \psi^{sc}}{\partial n} \right] (\mathbf{r}) - M_k [\psi^{sc}] (\mathbf{r}), \quad \mathbf{r} \in S. \quad (11)$$

Here the integral M_k is singular, and should be treated in the sense of principal value.

For room acoustics the boundary integral equation (BIE) (11) combined with the boundary condition (7) is sufficient to solve the problem. There is no need to introduce the treatment to avoid spurious resonances, that was proposed by [BMW71] for the external problem. The degeneracy of the BIE in that case is due to two reasons: first, that the surface is sound hard, and, second that the problem is external. For impedance boundary conditions with non-zero real part of ζ (4), these resonances do not arise. Even if the surface is sound-hard, the problems in the BIE solution is related to the resonance in the internal problem and is a numerical artifact. However, for internal domains such resonances are physical and should be handled by different means.

For impedance boundary conditions (7) the BIE can be written either for unknown ψ^{sc} ,

$$\frac{1}{2} \psi^{sc}(\mathbf{r}, k) + M_k [\psi^{sc}] (\mathbf{r}) + k L_k \left[\frac{1}{i\zeta} \psi^{sc} \right] (\mathbf{r}) = L_k [\gamma] (\mathbf{r}), \quad \mathbf{r} \in S, \quad (12)$$

or unknown $\partial \psi^{sc} / \partial n$,

$$\frac{1}{2} \frac{\partial \psi^{sc}}{\partial n}(\mathbf{r}, k) + \frac{1}{\zeta(\mathbf{r}, k)} M_k \left[\zeta \frac{\partial \psi^{sc}}{\partial n} \right] (\mathbf{r}) + \frac{k}{i\zeta(\mathbf{r}, k)} L_k \left[\frac{\partial \psi^{sc}}{\partial n} \right] (\mathbf{r}) = \frac{1}{2} \gamma(\mathbf{r}, k) + \frac{1}{\zeta(\mathbf{r}, k)} M_k [\zeta \gamma] (\mathbf{r}), \quad \mathbf{r} \in S. \quad (13)$$

If ζ is constant over frequency, the matrices, $A_k = \frac{1}{2} I + M_k + \frac{k}{i\zeta} L_k$, are the same in both formulations, while the right hand sides, $b = L_k [\gamma]$ and $b = \left(\frac{1}{2} I + M_k \right) [\gamma]$ are different (here I is the identity matrix). In our numerical experiments we observed faster convergence for the flexible GMRES procedure for Eq. (12) and slow or no convergence for Eq. (13) for large values of ζ , while the results, for convergent cases, were correct for both formulations. The direct BEM used in this paper is described in [GD09].

3.2 Indirect BEM

The indirect BEM can be used wherever the direct BEM can, and in addition for cases when the surface S is open (say a problem with an open door to the room, and with some thin baffles inside the room). The reason, why the direct BEM is preferable for closed rooms is that it leads to a more compact BIE. For open surfaces we must use a representation of the sound field via single and double layer potentials of unknown intensities σ and μ

$$\psi^{sc}(\mathbf{r}; k) = L_k[\sigma](\mathbf{r}) + M_k[\mu](\mathbf{r}), \quad \mathbf{r} \notin S. \quad (14)$$

These intensities can be determined from the boundary conditions and the jump conditions on the surface. Denote the side of S facing the inside as S^- and the side faced outside the room as S^+ . Using “+” and “-” superscripts for parameters on that surfaces we can write the jump conditions for field (15) as

$$\psi^{sc\pm}(\mathbf{r}; k) = L_k[\sigma](\mathbf{r}) + M_k[\mu](\mathbf{r}) \pm \frac{1}{2}\mu(\mathbf{r}, k), \quad \mathbf{r} \in S^\pm, \quad (15)$$

$$\frac{\partial}{\partial n}\psi^{sc\pm}(\mathbf{r}; k) = L'_k[\sigma](\mathbf{r}) + M'_k[\mu](\mathbf{r}) \mp \frac{1}{2}\sigma(\mathbf{r}, k), \quad \mathbf{r} \in S^\pm,$$

$$L'_k[\sigma](\mathbf{r}) = \int_S \sigma(\mathbf{r}') \frac{\partial}{\partial n(\mathbf{r})} G_k(\mathbf{r}, \mathbf{r}') dS(\mathbf{r}'), \quad (16)$$

$$M'_k[\mu](\mathbf{r}) = \frac{\partial}{\partial n(\mathbf{r})} \int_S \mu(\mathbf{r}') \frac{\partial}{\partial n(\mathbf{r}')} G_k(\mathbf{r}, \mathbf{r}') dS(\mathbf{r}'),$$

and the integral singularities for evaluation points on the surface are treated in terms of principal values. The normal is directed from “-” to “+” side of the surface.

Different variables can be declared as principal unknowns. For example, jump relations (15) and boundary conditions (7) allow us to express the system in terms of two variables ψ^{sc+} and ψ^{sc-} on sides S^+ and S^- , respectively, as we have (we drop arguments (\mathbf{r}, k) for all functions to shorten notation)

$$\begin{aligned} \mu &= \psi^{sc+} - \psi^{sc-}, & (17) \\ \sigma &= \frac{\partial}{\partial n}\psi^{sc-} - \frac{\partial}{\partial n}\psi^{sc+} = \gamma^- + \gamma^+ - \frac{k}{i\zeta^-}\psi^{sc-} - \frac{k}{i\zeta^+}\psi^{sc+}, \\ \pm \frac{\partial}{\partial n}\psi^{sc\mp} + \frac{k}{i\zeta^\mp}\psi^{sc\mp} &= \gamma^\mp = \mp \frac{\partial}{\partial n}\psi^{in\mp} - \frac{k}{i\zeta^\mp}\psi^{in\mp}, \end{aligned}$$

So, we have from Eq. (15)

$$\begin{aligned} &\frac{(\psi^{sc-} + \psi^{sc+})}{2} - M_k[\psi^{sc+} - \psi^{sc-}] + L_k\left[\frac{k\psi^{sc-}}{i\zeta^-} + \frac{k\psi^{sc+}}{i\zeta^+}\right] = L_k[\gamma^- + \gamma^+], & (18) \\ &-M'_k[\psi^{sc+} - \psi^{sc-}] + \frac{1}{2}\left(\frac{k\psi^{sc+}}{i\zeta^+} - \frac{k\psi^{sc-}}{i\zeta^-}\right) + L'_k\left[\frac{k}{i\zeta^-}\psi^{sc-} + \frac{k}{i\zeta^+}\psi^{sc+}\right] \\ &= \frac{1}{2}(\gamma^+ - \gamma^-) + L'_k[\gamma^- + \gamma^+]. \end{aligned}$$

Note that in contrast to the BIE equations (11), the equations (18) contain integrals L'_k and the hypersingular integral M'_k . In our conference communication [GAD13], we briefly described the indirect BEM from more general case than room acoustics. The details for computing the boundary integrals can be found in [GD21].

3.3 Fast multipole method

The FMM strategy for boundary element methods was discussed in [GD09]. According to that approach, the discretization should be selected in a way that approximation for far field integrals is good enough. The space partitioning with octree should be designed in a way that the size of the smallest box δ is larger than the cutoff distance, $\delta > r_c$. In this computation of matrix entries corresponding to the interactions between closely located elements can be done using analytical formulae, while far field interactions are obtained via regular FMM procedures involving multipole and local expansions and translations.

The FMM for the Helmholtz kernel used in the present study is the same as in [GD09]. It requires local-to-local (which are the same as multipole-to-multipole) translations for the Helmholtz equation even at large frequencies. Such translations are performed using the RCR-decomposition of translations (rotation, coaxial translation, and back rotation). We found that the recurrences for computation of the reexpansion coefficients proposed in our paper [GD04] and book [GD05] are not stable at large values of parameter kD , where D is the size of the computational domain (diagonal of the bounding cube). In our room computations presented in this paper kD may be the value of several thousands (which is also the order of magnitude for the degree of spherical harmonics). This relates both to rotations and coaxial translations. A conditionally stable recursive procedure for computation of the rotation operators, which is tested up to degrees of spherical harmonics 10^4 is presented in our study [GD15]. There exist other rotation methods tested for degrees of spherical harmonics of the order of 10^3 [GG09], which potentially can be used in the present method. Stabilization of the recursions for the coaxial translation coefficients is new.

3.3.1 Stable high frequency coaxial translations

In the FMM two types of representation of the solutions of the Helmholtz equation are considered, the local and the multipole (far field expansions). These expansions are

$$\begin{aligned} \psi(\mathbf{r}) &= \sum_{n=0}^{p-1} \sum_{m=-n}^n C_n^m S_n^m(\mathbf{r}), \quad \psi(\mathbf{r}) = \sum_{n=0}^{p-1} \sum_{m=-n}^n D_n^m R_n^m(\mathbf{r}), \\ S_n^m(\mathbf{r}) &= h_n(kr) Y_n^m(\mathbf{r}/r), \quad R_n^m(\mathbf{r}) = j_n(kr) Y_n^m(\mathbf{r}/r), \quad r = |\mathbf{r}|, \end{aligned} \quad (19)$$

where $S_n^m(\mathbf{r})$ and $R_n^m(\mathbf{r})$ are the singular and regular at $r = 0$ spherical basis functions, j_n and h_n are the spherical Bessel and Hankel functions of the first kind, and $Y_n^m(\mathbf{r}/r)$ are the spherical harmonics (we use definition which can be found in references [GD05, GD09, GD15]). The infinite summation over n is truncated to p , leading to p^2 coefficients. Each step of the FMM requires representation of the same function in a reference frame with a shifted origin compared to the original. This can be handled using reexpansions of the basis functions, which for translations along the z axis gives

$$S_n^m(\mathbf{r} + \mathbf{i}_z \tau) = \sum_{n=0}^{p-1} (S|R)_{n'n}^m(\tau) R_{n'}^m(\mathbf{r}), \quad R_n^m(\mathbf{r} + \mathbf{i}_z \tau) = \sum_{n=0}^{p-1} (R|R)_{n'n}^m(\tau) R_{n'}^m(\mathbf{r}), \quad (20)$$

where $(S|R)_{n'n}^m$ and $(R|R)_{n'n}^m$ are the coaxial reexpansion, or translation coefficients (we do not show here the $(S|S)_{n'n}^m(\tau)$ coefficients which are equal to $(R|R)_{n'n}^m(\tau)$ coefficients). The problem then is efficiently compute these coefficients.

The scheme for computation of the three-index coaxial translation coefficients $(E|F)_{n'n}^m$ (E and F can take any value S or R) proposed in [GD04] and [GD05] can be compacted to the following algorithm.

1. Compute zero-order sectorial coefficients for non-negative order m (the coaxial coefficients depend only on $|m|$)

$$\begin{aligned} (S|R)_{n'}^0(\tau) &= (-1)^{n'} \sqrt{2n'+1} h_{n'}(k\tau), \\ (R|R)_{n'}^0(\tau) &= (-1)^{n'} \sqrt{2n'+1} j_{n'}(k\tau), \\ (E|F)_{n'm}^m &= (E|F)_{n'm}^m, \quad n' = m, m+1, \dots, \quad E, F = S, R. \end{aligned} \quad (21)$$

2. Compute all other order sectorial coefficients

$$\begin{aligned} b_{m+1}^{-m-1} (E|F)_{n'}^{m+1} &= b_{n'}^{-m-1} (E|F)_{n'-1}^m - b_{n'+1}^m (E|F)_{n'+1}^m, \\ m &= 0, 1, \dots, \quad n' = m+1, m+2, \dots \end{aligned} \quad (22)$$

3. Compute the tesseral coefficients using relation

$$a_{n-1}^m (E|F)_{n',n-1}^m - a_n^m (E|F)_{n',n+1}^m = a_{n'}^m (E|F)_{n'+1,n}^m - a_{n'-1}^m (E|F)_{n'-1,n}^m. \quad (23)$$

The latter recursion is applied to compute coefficients in the range

$$m = 0, \dots, p-1, \quad n = m, \dots, p-2, \quad n' = n, \dots, 2p-2-n, \quad (24)$$

using propagation in n index

$$(E|F)_{n',n+1}^m = \frac{1}{a_n^m} \left[a_{n-1}^m (E|F)_{n',n-1}^m - a_{n'}^m (E|F)_{n'+1,n}^m + a_{n'-1}^m (E|F)_{n'-1,n}^m \right]. \quad (25)$$

4. Compute coefficients for $n' < n$ using symmetry

$$(E|F)_{n'n}^m = (-1)^{n+n'} (E|F)_{nn'}^m.$$

Numerical tests show that this scheme is unstable at large $k\tau$. They also show that steps 1) and 2) are stable, and the instability arises from step 3). To stabilise the recursive computation we modify the algorithm as follows. We use the existing scheme for $k\tau \lesssim 1$, and as a relatively small number of translation coefficients need be computed, the instability does not develop for reasonable computational accuracy (e.g., for double precision computing). For larger $k\tau \gtrsim 1$ instead of propagation in n index in step 3, see Eq. (25), we use propagation in the n' index,

$$(E|F)_{n'+1,n}^m = \frac{1}{a_{n'}^m} \left[a_{n-1}^m (E|F)_{n',n-1}^m - a_n^m (E|F)_{n',n+1}^m + a_{n'-1}^m (E|F)_{n'-1,n}^m \right], \quad (26)$$

$$m = 1, \dots, p-1, \quad n' = m+3, \dots, p-2, \quad n = m+1, \dots, n'-2.$$

For implementation some additional coefficients must be computed, namely the zonal and diagonal and subdiagonal coefficients. This introduces steps 3.1 and 3.2 which must be performed before step 3:

3.1 Compute zonal coefficients using propagation in n -direction for $n = 0, \dots, p-2, \quad n' = n+1, \dots, 2p-n-3$:

$$(E|F)_{n',n+1}^0 = \frac{1}{a_n^0} \left[a_{n-1}^0 (E|F)_{n',n-1}^0 - a_{n'}^0 (E|F)_{n'+1,n}^0 + a_{n'-1}^0 (E|F)_{n'-1,n}^0 \right]. \quad (27)$$

3.2 Compute diagonal and subdiagonal tesseral coefficients using propagation in m and in diagonals for $m = 0, 1, \dots, p-3$,

$$(E|F)_{n+1,n}^{m+1} = \frac{1}{b_{n+1}^{-m-1}} \left(b_{n+1}^m (E|F)_{n+1,n}^m + b_n^{-m-1} (E|F)_{n,n-1}^m - b_n^m (E|F)_{n,n-1}^{m+1} \right), \quad (28)$$

$$n = m+2, \dots, p-2,$$

$$(E|F)_{n+1,n+1}^{m+1} = \frac{1}{b_{n+1}^{-m-1}} \left(b_n^m (E|F)_{n+1,n-1}^{m+1} - b_{n+2}^m (E|F)_{n+2,n}^m + b_{n+1}^{-m-1} (E|F)_{n,n}^m \right),$$

$$n = m+1, \dots, p-2.$$

$$(E|F)_{n+2,n}^{m+1} = \frac{1}{b_{n+2}^{-m-1}} \left(b_{n+1}^m (E|F)_{nn}^{m+1} - b_{n+1}^m (E|F)_{n+1,n+1}^m + b_{n+1}^{-m-1} (E|F)_{n+1,n-1}^m \right),$$

$$n = m+2, \dots, p-2.$$

The reason for this modification of the original algorithm is in the stability analysis based on the Courant-Friedrichs-Lewy (CFL) criterion [CFL67]. In step 3 of the original algorithm, the instability manifests itself at large n and n' . We perform stability analysis for the following recursion

$$(E|F)_{n',n-1}^m - (E|F)_{n',n+1}^m = c \left[(E|F)_{n'+1,n}^m - (E|F)_{n'-1,n}^m \right]. \quad (29)$$

$$c \sim \frac{a_{n'}^m}{a_n^m} \sim \frac{n}{n'} \sqrt{\frac{n'^2 - m^2}{n^2 - m^2}}, \quad (n \gg 1, \quad n' \gg 1),$$

Considering n as time and n' as a spatial variable, then (29) is like a finite-difference scheme for the wave equation with celerity $-c$ and unit steps in the space and time. The CFL stability condition is $|c| \leq 1$, and so

$$\frac{n}{n'} \sqrt{\frac{n'^2 - m^2}{n^2 - m^2}} \leq 1, \quad \text{or } n \geq n'. \quad (30)$$

In the previous scheme the recursion was applied for computation of $(E|F)_{n',n+1}^m$ for $n' \geq n$, which means instability. The change in the direction of propagation fixes the problem. The computation of the zonal and diagonal/subdiagonal coefficients (step 3.1 and 3.2 of the modified algorithm) are neutrally or asymptotically stable. We implemented and tested the algorithm and found that it is stable and can be used for computations of the reexpansion coefficients of large degree. We also found that at low $k\tau$ the new algorithm exhibits a error due to summation of terms of essentially different magnitude, leading to loss of the precision. We thus propose the use of the original algorithm at low $k\tau$ and the modified algorithm for higher values of $k\tau$.

4 Room Acoustic Simulations

The BEM based on the theory presented above was implemented using Open MP parallelization and validated. The results discussed below are obtained on a workstation equipped with two Intel E5-2683 16 core processors @2.1 GHz and 128 GB RAM.

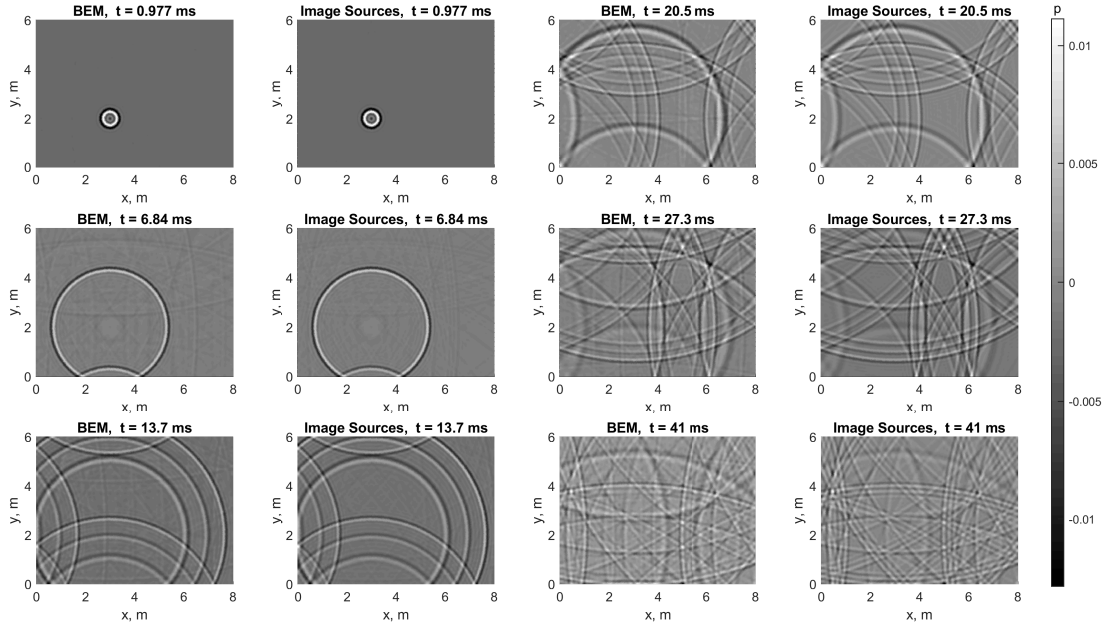


Figure 1: A side-by-side comparison of the solutions at $z = 1.75$ m obtained at different times using the direct BEM and the method of image sources for a pulse (33) from a source in a rectangular $8 \times 6 \times 3$ m room. The coordinates of the source are $(3, 2, 1.75)$ m. The reflection and absorption coefficients are $R = 0.8$ and $\alpha = 0.36$, respectively. Computations performed for 128 frequencies and converted to the time domain using the FFT.

4.1 Comparisons with analytical solution

For validation of the BEM we use analytical solution for a monopole source located at $\mathbf{r} = \mathbf{r}_s$ inside a rectangular room [AB79],

$$p(\mathbf{r}, t) = \frac{1}{|\mathbf{r} - \mathbf{r}_s|} f\left(t - \frac{1}{c} |\mathbf{r} - \mathbf{r}_s|\right) + \sum_j \frac{A_j}{|\mathbf{r} - \mathbf{r}_j|} f\left(t - \frac{1}{c} |\mathbf{r} - \mathbf{r}_j|\right), \quad (31)$$

where $f(t)$ is a given function of time, and \mathbf{r}_j are locations of the image sources of relative amplitude $A_j = R^{n_j}$, where R is the reflection coefficient and n_j the index of the image equal to the minimal

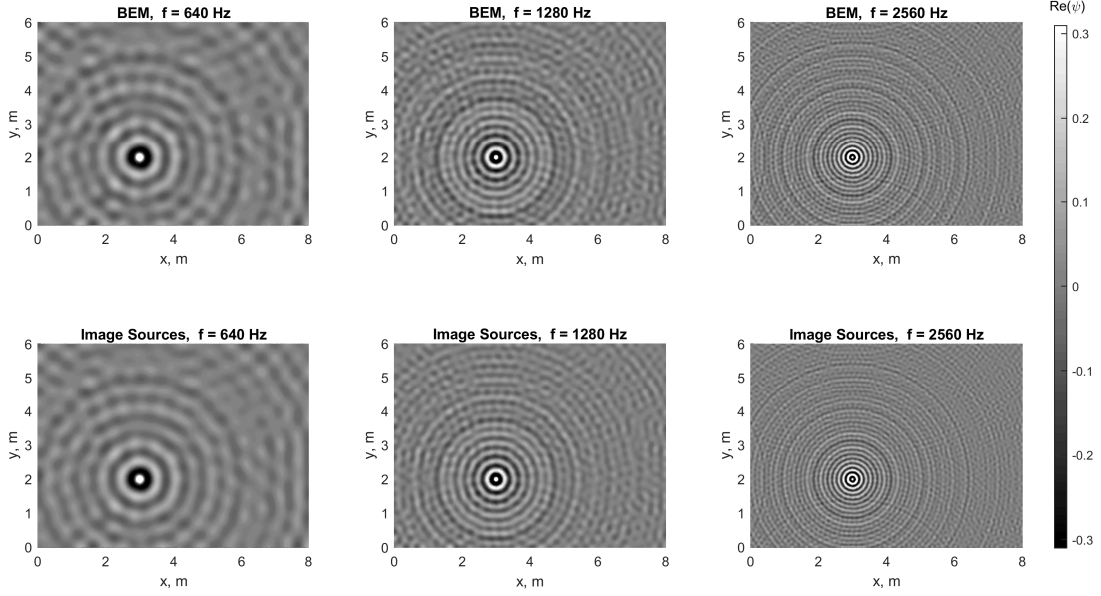


Figure 2: A comparison of the solutions described in Fig. 1 in the frequency domain at three different frequencies.

number of reflections to obtain the image. For a solution limited in time as $0 \leq t \leq T_{\max}$, only sources within radius $|\mathbf{r} - \mathbf{r}_j| < cT_{\max}$ from evaluation point \mathbf{r} can be considered. Also the sources of intensity A_j below some threshold, A_{th} , can be ignored (in our computations we used $A_{th} = 10^{-7}$). For comparisons of solutions in the frequency domain we also computed

$$\psi(\mathbf{r}, k) = G_k(\mathbf{r}, \mathbf{r}_s) + \sum_j A_j G_k(\mathbf{r}, \mathbf{r}_j), \quad (32)$$

for each frequency. For comparisons with the analytical solution the latter is generated for a room of dimensions $(l_x, l_y, l_z) = (8, 6, 3)$ m with wall reflection coefficient $R = 0.8$. A monopole sound source is placed at $\mathbf{r}_s = (3, 2, 1.75)$ m. For the function of time we used

$$f(t) = \delta_f(t - \Delta t) - \delta_f(t + \Delta t), \quad \delta_f(t) = \begin{cases} 1, & t = 0 \\ 0, & t \neq 0 \end{cases} \quad (33)$$

where δ_f is a finite version of the Dirac delta-function. In the example shown below we used $T_{\max} = 50$ ms, and $\Delta t = T_{\max}/256$. All time values were interpolated to a time grid with step Δt using the closest neighbor value for shifted $f(t)$. We also computed solution (32) for 128 equispaced frequencies from 20 to 2560 Hz. The results then were convolved with $f(t)$ using the FFT for each evaluation point. We found good agreement between the frequency and time domain computations, while some differences were explainable due to the interpolation in the time domain. For further comparisons with the BEM we used frequency domain computations.

The direct BEM for the Helmholtz equation with boundary conditions (7), where $\zeta = 9$ ($\alpha = 1 - R^2 = 0.36$, see Eq. (4)) was applied to get solution for all 128 frequencies. The room surface was discretized with a mesh containing $N = 1,806,532$ triangles with the maximum edge length 2 cm, which provided resolution at least 6.7 elements per wavelength at the highest computed frequency. The field was evaluated at 241,542 grid points in a plain located at the height of the source ($z = 1.75$ m) and covering the entire area of the room. The results of computations were converted to the time domain as described above and compared with the method of image sources.

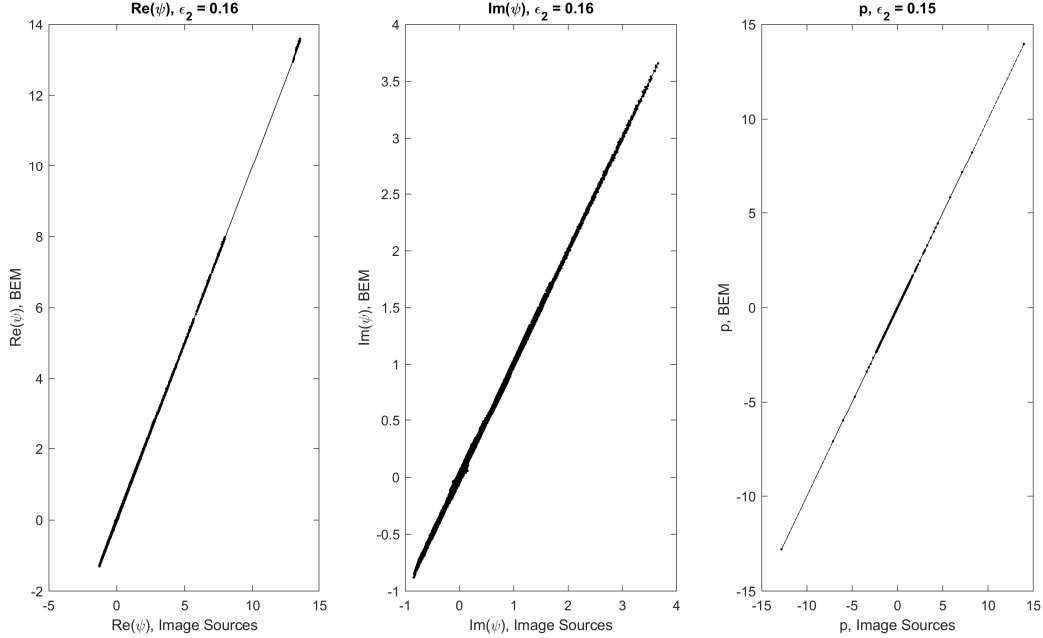


Figure 3: Comparisons of the real and imaginary parts of the complex amplitude of the acoustic pressure obtained by the direct BEM and the image source method for all 128 frequencies and all evaluation points used for computing the images (on the left and in the center). A comparison for acoustic pressure at 256 different time instances and all evaluation points is shown on the rightmost graph.

Figure 1 shows comparisons of the results of the BEM and the image source method in time domain. The time frames show excellent agreement and clear physical interpretation of the results. At $t = 0.977$ ms one can see a simple spherical wavefront, which at the next time frame shown interacts with the wall and the reflected wave is seen. Also, at $t = 6.84$ ms one can see a dark spot near the source location, which is due to the wave reflected from the ceiling. The next time frame illustrates shows three wave fronts (triplet) interacting with the walls. The wave front with the largest radius here is due to the real source, while the two following wavefronts of smaller radii are due to reflections from the ceiling and the floor, respectively. At $t = 20.5$ ms one can see more reflections of the triplet of the wavefronts and also a stronger single spherical front propagating from the source location and reflected by the walls. This wavefront is a superposition of the waves due to the secondary images located under the floor and above the ceiling, which arrival time to the imaging plane is the same. The last two figures show more reflections. One can also observe the decay in the intensity of multiple reflected waves.

Figure 2 illustrates the frequency domain computations at three selected frequencies, which were used for synthesis of the time domain solution. Again, one can see a good agreement between the computations using different methods, while the wave pattern is quite complex due to multiple reflections.

Figure 3 compares point-by-point the analytical and BEM solutions in the frequency domain for all 128 frequencies (the total number of data points 30,917,376 complex numbers) and in the time domain (61,834,752 real numbers) for all 256 times. It is seen that the agreement is good, as ideally, all points should fall on the line $y = x$. The relative L_2 -norm error is 16% for frequency domain and 15% for time domain data.

We relate this difference to the boundary conditions used in the BEM and in the method of images. Indeed, in the BEM we use impedance conditions (3), which are conditions for the locally reacting surface, while the method of images for absorbing walls, in fact, corresponds to the conditions depending on the angle of incidence [Kut16]. For specific impedance $\zeta = 0.9$ the deviation of the both types of conditions from sound-hard boundary conditions can be of the order of 10% or so. Note that for time domain the errors are of the order of a few percents for relatively small times when there are no

reflections. Hence, 15% difference between the solutions should not be surprising, while the qualitative agreement of the solution features is encouraging.

4.2 More complex rooms

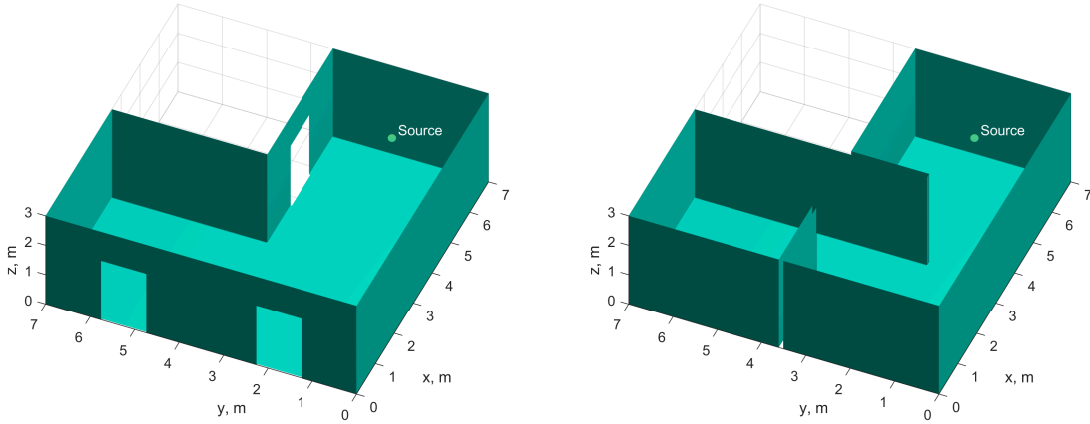


Figure 4: Configurations of the L-shaped room used in simulations with open doors and with baffles (configurations of the room with closed doors/no baffles and without baffles/open doors are not shown). The room can be thought as a box of dimensions $7 \times 7 \times 3$ m, from which a box of dimensions $3.5 \times 3.5 \times 3$ m is extracted. The coordinates of the source are $(6, 1.75, 1.75)$ m.

L-shaped room Further, we conducted computations for more complex rooms, such as shown in Fig. 4. Computations for the case shown in Fig. 4 on the left with the doors closed are shown in Fig. 5. Two sets of computations for two different meshes were performed. First, for the mesh with the maximum edge 1 cm (6,310,256 triangles), and, second, for the mesh with the maximum edge 2 cm (1,579,544 triangles). The first mesh was used for computations for frequencies up to 5.12 kHz ($kD \approx 1137$), while the second mesh was used for computations for frequencies up to 2.56 kHz ($kD \approx 569$). This corresponds to the mesh resolution of 6.7 elements per wavelength for the highest frequency. In both cases the reflection coefficient was set to a constant $R = 0.9$ ($\alpha = 0.19$, $\zeta = 19$). The time domain data are obtained as in the case for the rectangular room using the FFT for 256 and 128 frequencies equispaced from 20 Hz to the maximum frequency. Note that the case for a finer mesh is evaluated on a finer grid consistent with the mesh vertices.

Figure 5 compares time domain computations for two cases for pulses described by Eq. (33). The comparison shows agreement between the two data sets, while computations on finer mesh provide sharper pictures. We also compared computations using the direct and indirect methods. Figure 6 compares side-by-side simulations using these methods in the frequency domain for 2.56 kHz. It is hard to find any difference visually, while the difference of about 4.5% in the relative L_2 -norm exists. Such level of the errors can be related to the BEM itself (discretization, approximation of far-field integrals, etc.). The comparison can be used as cross-validation of the direct and indirect methods.

Room with openings Opening in a room such as open doors, windows or ventilation outlets can be modeled in two ways. The more natural way is to use the indirect BEM, which can handle open surfaces. Another way is to use the direct BEM with proper boundary conditions imposed on the regions of

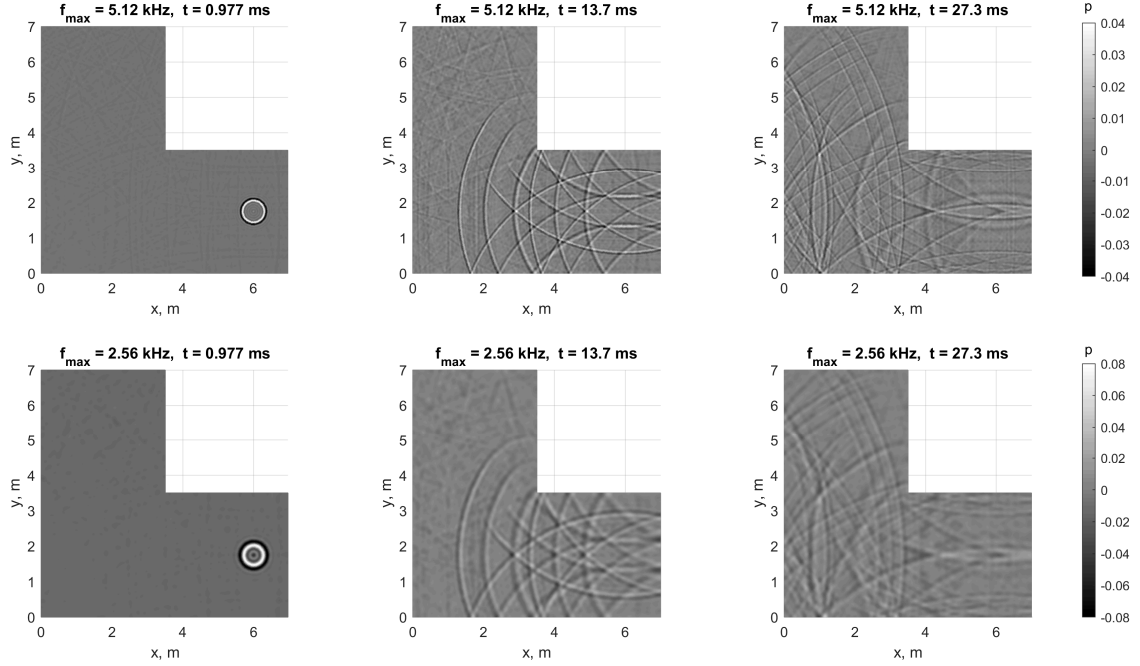


Figure 5: Comparisons of the direct BEM computations at $z = 1.75$ m and different times for the L-shaped room with closed doors using different spatial and temporal resolutions: a) mesh with 1 cm max element size and 256 frequencies from 20 Hz to 5.12 kHz (the upper row); b) mesh with 2 cm max element size and 128 frequencies from 20 Hz to 2.56 kHz (the bottom row). The reflection and absorption coefficients are $R = 0.9$ and $\alpha = 0.19$. Patterns in time domain obtained using convolution of the pulse (33) and frequency domain computations.

openings. For example, one can assign to the impedance boundary condition (3) with specific impedance $\zeta = 1$, which corresponds to the reflection coefficient $R = 0$ (absorption $\alpha = 1$, see Eq. (4)).

Figure 7 illustrates computations for the same 2 cm resolution (maximum frequency 2.56 kHz) as in the case illustrated in Fig. 5 ($R = 0.9$ on the entire surface). Here the cases with the doors closed and open are compared and overall difference of 20% in the relative L_2 -norm found (all receiver points over all times). While the wave patterns look similar for these two cases, one can notice some differences near the door regions, as the reflected waves in the case of closed doors are stronger. This difference is better seen as we plot the difference between the cases of open and closed doors shown in Fig. 8 in the frequency domain. Here one can see that the difference is equivalent to the effect of sound sources distributed over the opening areas. Also, on the same figure we displayed the difference between the cases of open and closed doors computed using the indirect BEM. It is seen that the wave patterns for the direct and indirect BEM simulations are the same. Nonetheless, there exists a difference of about 8% between computations obtained by the two methods, which is larger than the expected BEM errors. This difference is also illustrated in Fig. 8 and is associated with the fact that boundary conditions (3) with specific impedance $\zeta = 1$ are not fully absorbing (they are fully absorbing only for the waves of normal incidence). So, some discrepancy between the direct BEM with conditions (3) and indirect BEM (the latter corresponds to truly full absorption) should exist and we observe it in our computations. Note here, that for modeling of openings some other boundary conditions and methods instead of Eq. (3) can be used, for example, one can consider utilization of perfectly matched layers, which is common for computations of wave equations in open domains.

Room with baffles The presence of baffles drastically changes the acoustic field in the room. For computational examples we used the L-shape room with closed doors shown in Fig. 4. The reflection

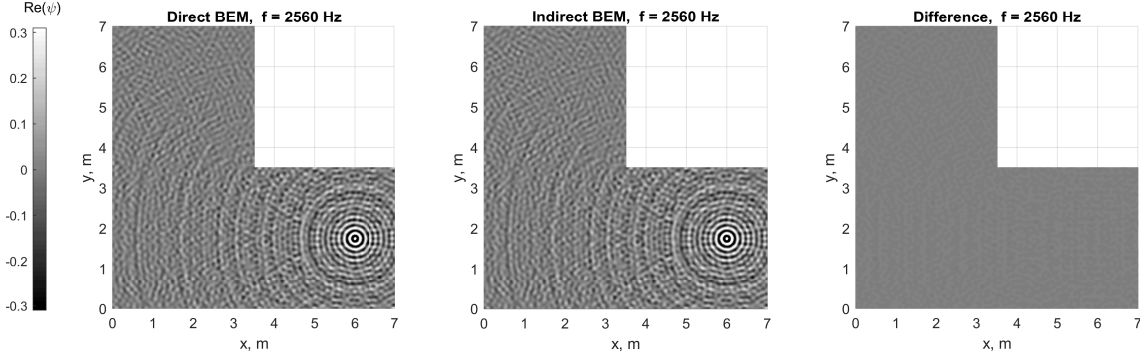


Figure 6: Comparisons of the direct and indirect BEM computations at $z = 1.75$ m for the L-shaped room with closed doors at $f = 2.56$ kHz, $R = 0.9$ and $\alpha = 0.19$.

coefficient is $R = 0.9$ for the entire room, while we assumed that the baffles are fully absorbing, $R = 0$. Again, two methods were used for computations and analysis, the direct and indirect BEM. In the direct BEM the thickness of baffles is 7 cm, while in the indirect method the baffles are treated as infinitely thin objects.

Figure 9 illustrates several frames in the time domain obtained using direct BEM executed for a 2 cm resolution mesh and maximum frequency 2.56 kHz. The frame at $t = 8.2$ ms shows the principal wave and its reflections from the walls (thin wave fronts) and from the ceiling (thick wave fronts). It also shows interaction of the main wave with the baffle, as only part of the wave goes through the opening, while rather weak reflection is observed from the baffle itself. This also confirms that the baffle does not absorb the wave perfectly as the angular dependence of the reflection coefficient is ignored in the model. However, for the frames at later stages the reflections from the baffles are not observed clearly, which also can be related to substantial damping of such reflections from the image sources. Also, we analyzed wave patterns for several frequencies and could not see visually substantial reflections from the baffles. Examples of such patterns obtained using the direct and indirect BEM are shown in Figure 10 for frequency 2.56 kHz. Note that visually computations for the direct and indirect methods are very similar, but, in fact, the difference of 16% in the relative L_2 -norm exists. Such difference cannot be explained neither by the BEM accuracy, nor the models of reflection, as for both methods we used the same impedance boundary conditions with $\zeta = 1$ on the baffles.

The explanation comes from the consideration of the difference of the fields computed by the two methods also illustrated in Fig. 10. One can clearly see some pattern reminding a reflection from the baffle closest to the source. We relate this to the thickness of the baffle. Indeed, at 2.56 kHz the wavelength is 13.4 cm, so the baffle is approximately half-wavelength thick. By satisfying boundary conditions on the baffles we should observe that the crests and the troughs of the reflected waves near the offset baffle points should be exchanged and amplified in the difference figure. Note that we could not see any regular patterns in Fig. 6 illustrating the difference between the two methods for a room without baffles.

4.3 Performance

Some remarks can be made concerning the performance of the solvers. In most cases we computed using the direct BEM formulation (12) provided much better convergence than (13). Figure 11 illustrates wall-

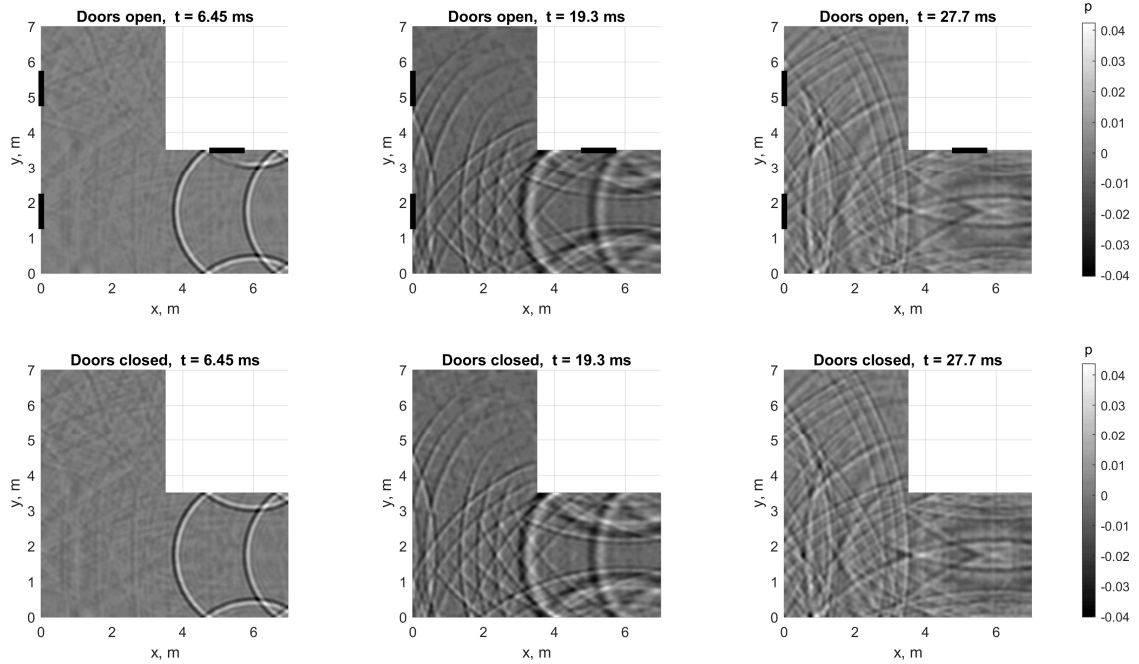


Figure 7: Comparisons of the direct BEM computations at $z = 1.75$ m and different times for the L-shaped room with closed and open doors. The reflection and absorption coefficients are $R = 0.9$ and $\alpha = 0.19$. The doors are modelled as regions with $R = 1$ and $\alpha = 0$.

clock times using two different meshes for L-shape room (for the case illustrated in Fig. 4). At fixed frequency the FMM is scaled almost linearly with respect to N (more precisely, as $O(N \log^m N)$, $m > 0$). As the mesh with resolution 1 cm contains 4 times more elements than the mesh with resolution 2 cm, ideally the solution time should be 4 times larger for the finer mesh. The ratio of the observed wall-clock times required for solution varies around this value (as the solution itself depends also on the number of matrix-vector calls in the iterative processes). Figure 11 also shows that at higher frequencies the wall-clock times, w , for the present algorithm are fitted well with a fit $w \sim a + bf^2$, where f is the frequency. Theoretically at fixed N and constant number of iterations the scaling for the present algorithm should be $w \sim a + bf^2 + cf^3$ with relatively small constant c [GD09].

Figure 12 illustrates various factors affecting the performance. The figure on the left panel shows that the performance of the direct BEM for the L-shape room with closed and open doors approximately the same. However, the times for computation of the room with the baffles can be several times larger. Note that the computation times are substantially affected by settings of the flexible GMRES preconditioned with the low accuracy FMM GMRES, such as the tolerance for convergence, the dimensionality of the Krylov subspaces, the number of iterations for the preconditioner, and the accuracy of the FMM used in the main and in the preconditioning loops [GD09]. The data plotted in the figure are obtained by taking the fastest times from several runs with different parameter settings. While this can be considered as some manual optimization, a systematic study of optimal parameters for the iterative solvers is required. The figure on the right panel of Fig. 12 shows the effect of the absorption coefficient α on the wall-clock time. It is seen that for low frequencies like 40 Hz the computation time just slightly depends on α . Such dependence is much stronger for larger frequencies and the wall-clock times at $\alpha \sim 0.01$ can be an order of magnitude larger than those at $\alpha \sim 1$. This figure also shows that at fixed α the frequency dependence of the wall-clock time can be non-monotonic. Note also that the wall-clock times for indirect BEM at large enough α are of the same order of magnitude as for the direct BEM, while for smaller α they can be much larger. Moreover, one may need to use some additional or different preconditioners in this case (we used a simple diagonal preconditioner (a constant diagonal added to the preconditioner matrix)).

Finally, we note that the present approach has a great opportunity for easy distributed parallelization

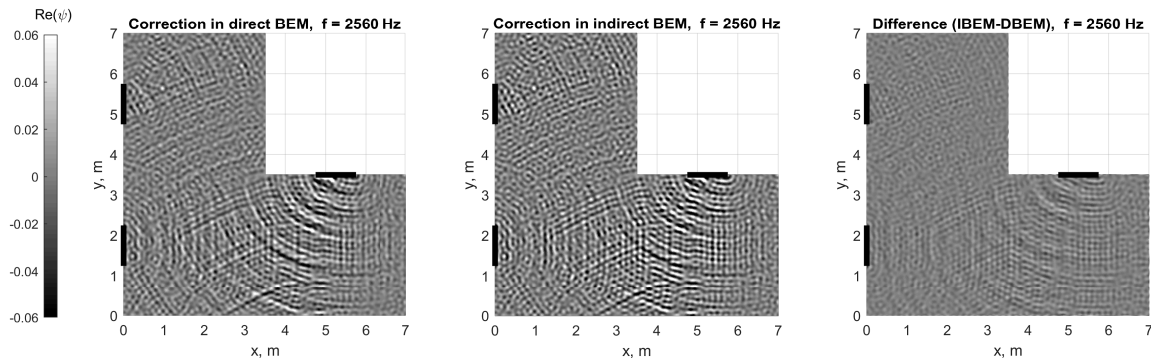


Figure 8: Correction to the closed door L-shaped room simulations to account for open doors when using the direct and indirect BEM at $z = 1.75$ m, $f = 2.56$ kHz, $R = 0.9$ and $\alpha = 0.19$. In the direct BEM the doors are modelled as regions with $R = 1$ and $\alpha = 0$. The chart on the right shows the difference between the indirect and direct BEM computations.

as the solution at different frequencies can be obtained independently on different computing nodes of a cluster. For example, Fig. 11 shows that for any of 128 frequencies computations on the 2 cm resolution mesh took less than 300 seconds. This means that a cluster of 128 nodes similar to our workstation can solve the entire problem for 300 seconds or so (in fact, a smaller number of nodes can be used for this and other cases as some nodes can perform two or more jobs; also, some optimization problems for job distributions can be considered).

5 Conclusion

Our computations, comparisons, and analysis show that the boundary element methods can be used for simulation of room acoustics for small rooms $V \sim 150$ m³. There are a number of advantages for the use of the BEM for room acoustics as this method is free from a number of deficiencies of the methods based on geometric acoustics approximation, provides a comprehensive information about the sound fields inside a room, and enables accounting for frequency dependent spatially varying absorption. Comparisons with the image source method for a rectangular room shows that the neglect of the angular dependence of the impedance generates a relatively small error in the solution of the order of 15%. Computations for an L-shaped room show that the effects of openings such as doors can be of the order of 20%. Modeling of baffles should be done with care as the thickness of baffles can cause 15% difference at wavelengths comparable with the baffle thickness.

Our numerical experiments also show that a proper form of the boundary integral equation should be selected for the direct method. The difference in performance heavily depends on this formulation. As a rule, for low absorptions the indirect BEM shows much slower convergence than the direct BEM. Furthermore, there are many factors affecting the BEM performance, such as the presence of baffles and the value of the absorptions coefficient. It is also important to find some optimal settings for iterative solver. Tuning of the solver parameters can improve performance several times. While in some cases the convergence of the BEM is excellent and the problem for the entire frequency range can be solved on computational clusters for 5 min or so, there exist cases of slow convergence, which require more detailed studies, and probably design of good preconditioners.

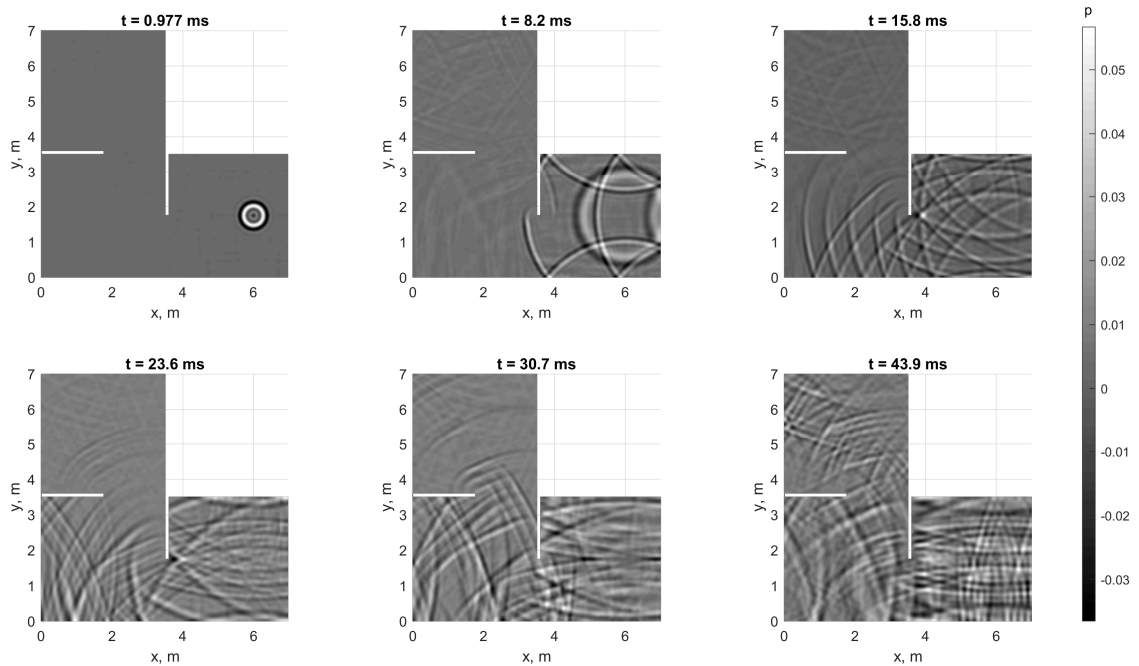


Figure 9: Direct BEM computations of pulse (33) propagation in the L-shaped room with baffles (closed doors) at $z = 1.75$ m and different times. The reflection and absorption coefficients are $R = 0.9$ and $\alpha = 0.19$ everywhere but on the baffles at which $R = 0$ and $\alpha = 1$. Computations performed for 128 frequencies from 20 Hz to 2.56 kHz and converted to the time domain using the FFT.

Acknowledgments

This research was conducted at VisiSonics Corporation.

References

- [AB79] Jont B Allen and David A Berkley. Image method for efficiently simulating small-room acoustics. *J. Acoust. Soc. Am.*, 65(4):943–950, April 1979.
- [BHBS16] S Bilbao, B Hamilton, J Botts, and L Savioja. Finite volume time domain room acoustics simulation under general impedance boundary conditions. *IEEE/ACM Transactions on Audio, Speech, and Language Processing*, 24(1):161–173, January 2016.
- [BMW71] A J Burton, G F Miller, and James Hardy Wilkinson. The application of integral equation methods to the numerical solution of some exterior boundary-value problems. *Proc. R. Soc. Lond. A Math. Phys. Sci.*, 323(1553):201–210, June 1971.
- [Bor84] Jeffrey Borish. Extension of the image model to arbitrary polyhedra. *J. Acoust. Soc. Am.*, 75(6):1827–1836, June 1984.
- [CFL67] R Courant, K Friedrichs, and H Lewy. On the partial difference equations of mathematical physics. *IBM J. Res. Dev.*, 11(2):215–234, March 1967. (English translation of original (in German) work “Über die partiellen Differenzgleichungen der mathematischen Physik,” *Mathematische Annalen*, 100(1), 32–74, 1928).
- [FTC⁺04] Thomas Funkhouser, Nicolas Tsingos, Ingrid Carlbom, Gary Elko, Mohan Sondhi, James E West, Gopal Pingali, Patrick Min, and Addy Ngan. A beam tracing method for interactive architectural acoustics. *J. Acoust. Soc. Am.*, 115(2):739–756, February 2004.

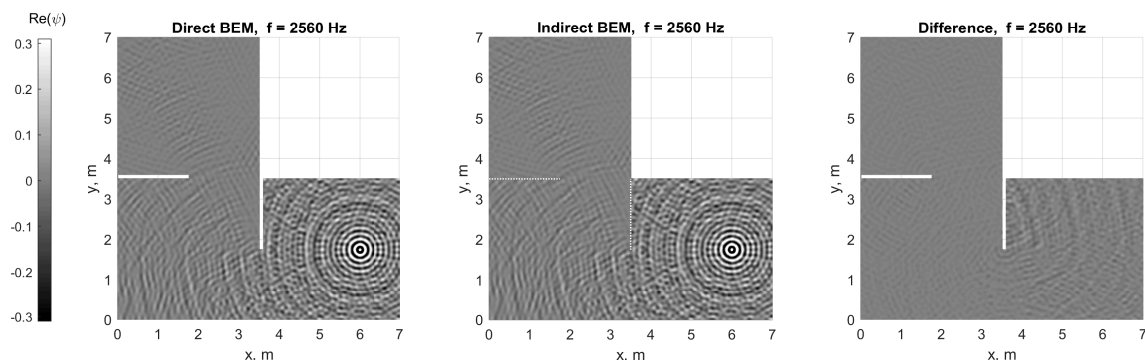


Figure 10: Comparisons of the direct and indirect BEM computations at $z = 1.75$ m for the L-shaped room with baffles (closed doors) at $f = 2.56$ kHz, $R = 0.9$ and $\alpha = 0.19$ ($R = 0$ and $\alpha = 1$ on the baffle). For the direct BEM, the thickness of the baffle is 7 cm.

- [GAD13] N Gumerov, R Adelman, and R Duraiswami. Fast multipole accelerated indirect boundary elements for the Helmholtz equation. *Proc. Meet. Acoust.*, 2013.
- [GD04] N A Gumerov and R Duraiswami. Recursions for the computation of multipole translation and rotation coefficients for the 3-D Helmholtz equation. *SIAM J. Scientific Computing*, 2004.
- [GD05] N A Gumerov and R Duraiswami. *Fast multipole methods for the Helmholtz equation in three dimensions*. Elsevier, 2005.
- [GD09] Nail A Gumerov and Ramani Duraiswami. A broadband fast multipole accelerated boundary element method for the three dimensional Helmholtz equation. *J. Acoust. Soc. Am.*, 125(1):191–205, January 2009.
- [GD15] N A Gumerov and R Duraiswami. Recursive computation of spherical harmonic rotation coefficients of large degree. In Radu Balan, Matthew Begué, John J. Benedetto, Wojciech Czaja, and Kasso A. Okoudjou, editors, *Excursions in Harmonic Analysis*. Springer, 2015.
- [GD21] Nail A. Gumerov and Ramani Duraiswami. Analytical computation of boundary integrals for the Helmholtz equation in three dimensions. *ArXiv*, 2021.
- [GG09] Z Gimbutas and L Greengard. A fast and stable method for rotating spherical harmonic expansions. *J. Comput. Phys.*, 228(16):5621–5627, September 2009.
- [GODZ10] Nail A Gumerov, Adam E O’Donovan, Ramani Duraiswami, and Dmitry N Zotkin. Computation of the head-related transfer function via the fast multipole accelerated boundary element method and its spherical harmonic representation. *J. Acoust. Soc. Am.*, 127(1):370–386, 2010.
- [HB17] B Hamilton and S Bilbao. FDTD methods for 3-D room acoustics simulation with High-Order accuracy in space and time. *IEEE/ACM Transactions on Audio, Speech, and Language Processing*, 25(11):2112–2124, November 2017.
- [Kut16] Heinrich Kuttruff. *Room Acoustics*. CRC Press, October 2016.
- [OYSO16] Takeshi Okuzono, Takumi Yoshida, Kimihiro Sakagami, and Toru Otsuru. An explicit time-domain finite element method for room acoustics simulations: Comparison of the performance with implicit methods. *Appl. Acoust.*, 104:76–84, March 2016.

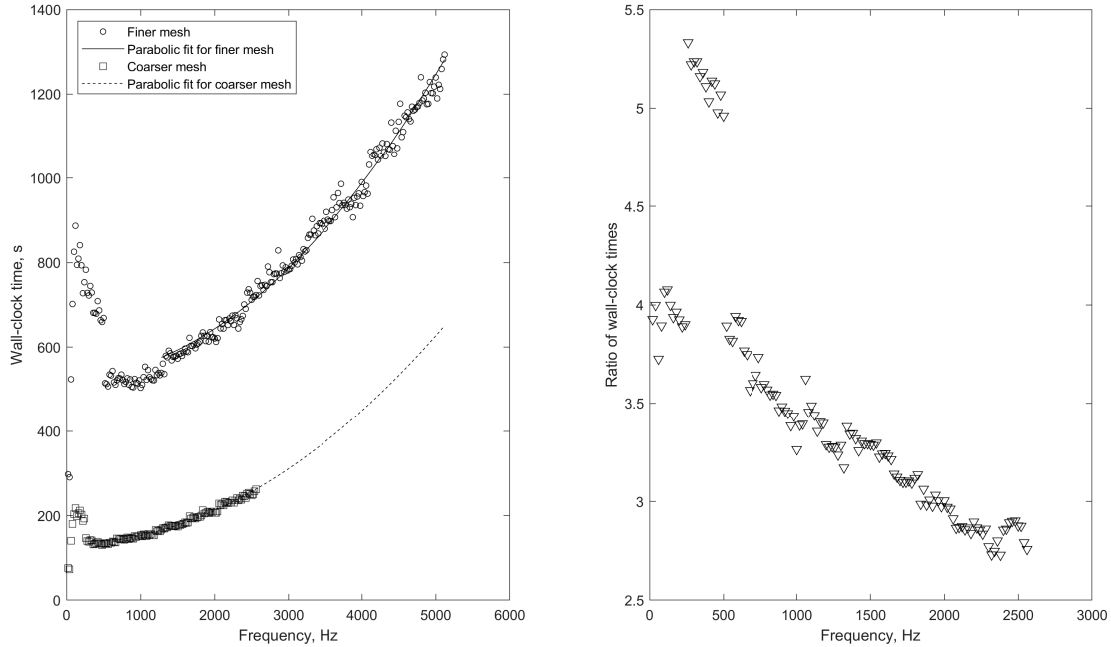


Figure 11: On the left: the wall-clock times required for direct BEM simulations for the L-shaped room with closed doors at different frequencies and different mesh sizes, $N = 6, 310, 256$ triangles (maximum edge 1 cm) and $N = 1, 579, 544$ triangles (maximum edge 2 cm), $R = 0.9$ and $\alpha = 0.19$. The continuous lines show parabolic fits On the right: the ratio of the wall-clock times for the higher and lower mesh resolutions.

- [PCD20] Samuel F Potter, Maria Cameron, and Ramani Duraiswami. Numerical geometric acoustics. *J. Acoust. Soc. Am.*, 148(4):2693–2693, October 2020.
- [RNL09] Nikunj Raghuvanshi, Rahul Narain, and Ming C Lin. Efficient and accurate sound propagation using adaptive rectangular decomposition. *IEEE Trans. Vis. Comput. Graph.*, 15(5):789–801, September 2009.
- [RS18] Nikunj Raghuvanshi and John Snyder. Parametric directional coding for precomputed sound propagation. *ACM Trans. Graph.*, 37(4):1–14, July 2018.
- [SMM14] Carl Schissler, Ravish Mehra, and Dinesh Manocha. High-order diffraction and diffuse reflections for interactive sound propagation in large environments. *ACM Trans. Graph.*, 33(4):1–12, July 2014.
- [SS15] Lauri Savioja and U Peter Svensson. Overview of geometrical room acoustic modeling techniques. *J. Acoust. Soc. Am.*, 138(2):708–730, August 2015.
- [ZDD04] D N Zotkin, R Duraiswami, and L S Davis. Rendering localized spatial audio in a virtual auditory space. *IEEE Trans. Multimedia*, 6(4):553–564, August 2004.

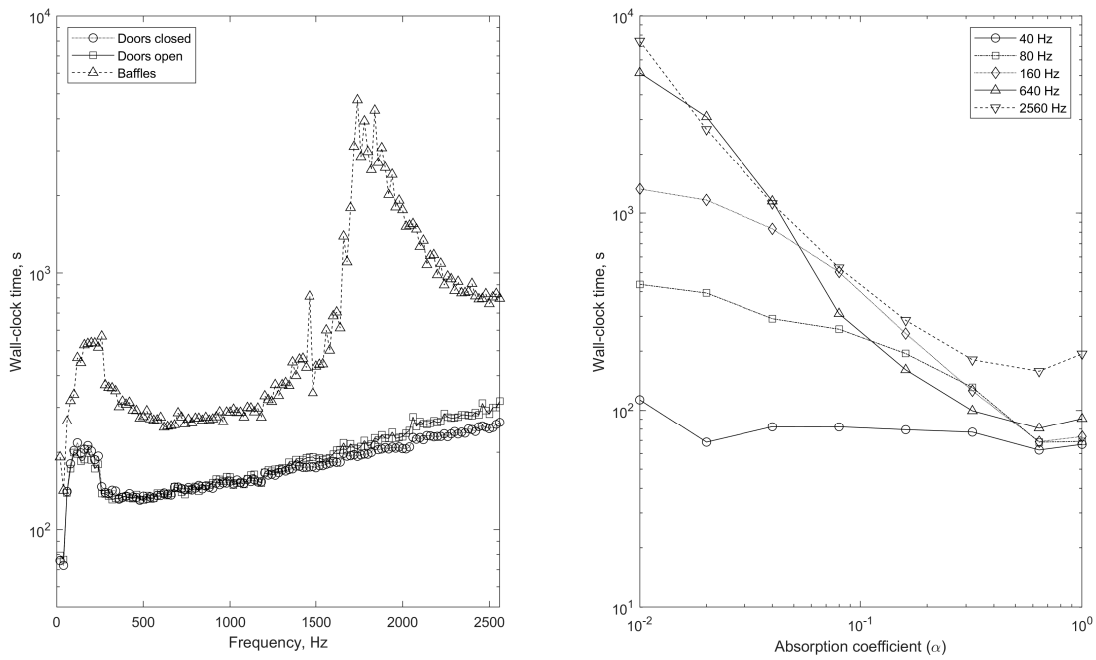


Figure 12: The influence of different factors on the time required for solution. On the left: the wall-clock time vs frequency required for the direct BEM solution of different configurations of the L-shaped room. On the right: the dependence of the direct BEM solution time for the L-shaped room with closed doors on the absorption coefficient α .